PERFORMANCE ENHANCEMENT BY EXPLOITING GEOMETRICAL NONLINEARITY OF INERTERS IN A TWO-STAGE VIBRATION ISOLATOR

Wei Dai

School of Naval Architecture and Ocean Engineering, Huazhong University of Science and Technology, Wuhan, 430074, P. R. China
daiwei699@hust.edu.cn

Baiyang Shi

Department of Engineering Design and Mathematics, University of the West of England, Bristol, BS16 1QY, United Kingdom.
baiyang.shi@uwe.ac.uk

Tianyun Li

School of Naval Architecture and Ocean Engineering, Huazhong University of Science and Technology, Wuhan, 430074, P. R. China
ltyz801@hust.edu.cn

Xiang Zhu

School of Naval Architecture and Ocean Engineering, Huazhong University of Science and Technology, Wuhan, 430074, P. R. China
zhuxiang@hust.edu.cn

Jian Yang*

Department of Mechanical, Materials and Manufacturing Engineering, University of Nottingham Ningbo China, Ningbo, 315100, P. R. China
jian.yang@nottingham.edu.cn

Received Day Month Year
Revised Day Month Year

This research proposes a two-stage vibration isolation system (TS-VIS) exploiting geometrical nonlinearity by inerters for performance enhancement. Lateral inerters are added to upper and lower stages creating geometric nonlinearity. The transmissibility and power flow indices are obtained for the performance evaluation. It is demonstrated that the inerters in both stages of the TS-VIS can enhance substantially the effectiveness of isolation at low frequencies by bending and shifting the resonance peaks in the force and energy transmission curves to the left while reducing the peak heights in these curves. It shows the use of inerters introduces a local minimum in the transmissibility curve which can be exploited for significant reduction in vibration transmission at a desirable frequency. By tailoring the inertance ratios for both stages of the TS-VIS, further improvements on the performance can be achieved by extending the frequency range of effective isolation. This work shows the benefits of using nonlinear inerters in the TS-VIS to obtain superior low-frequency isolation performance, which is potentially applicable in engineering systems such as floating raft structures.

Keywords: Inerter; Nonlinear vibration isolator; Power flow; Force transmissibility; Geometric nonlinearity.

* Corresponding author

1. Introduction

Vibration isolators are in great demand for efficient suppression of low-frequency vibration transmission from operating machines to foundation structures in automobile and marine engineering [Qiu *et al.*, 2022]. For example, excessive vibrations induced by the hosts and auxiliary machineries in underwater vehicles can be transmitted via the mounting structure to the hull resulting in structure-borne noise [Chen *et al.*, 2021]. Effective isolations and absorptions of low-frequency vibration are needed to reduce vibration transmission and noise radiation [Yang *et al.*, 2021; Zhang *et al.*, 2021]. For a conventional spring-mass-damper isolator having natural frequency of ω_{n}, effective isolation is achieved when the excitation frequency $\omega > \sqrt{2}\omega_{\mathrm{n}}$ [Ye and Ji, 2022]. Therefore, a compromise has to be made between having a low stiffness for low-frequency isolation and having a high stiffness for good load-carrying capacity [Niu and Chen, 2022].

To achieve better performance than that of linear isolators, geometric nonlinearities have been exploited in the designs of passive vibration isolators for superior performance. For instance, quasi-zero-stiffness (QZS) structures containing lateral linear springs [Zhao *et al.*, 2020] and linkage mechanisms comprising rigid rods and springs were proposed [Wang *et. al.*, 2020; Dai *et al.*, 2021]. Geometrically nonlinear structures can be used to provide negative dynamic stiffness so that a low linearized natural frequency [Yan *et al.*, 2022] is obtained. Recent studies have shown that compared to the linear and single-stage nonlinear isolation systems, a nonlinear two-stage vibration isolation system (TS-VIS) can have performance benefits by providing a wider effective isolation frequency band [Li and Xu, 2018]. Lu *et al.*, [2016] proposed a nonlinear QZS-based TS-VIS and found the isolation frequency band is enlarged. Wang and Li *et al.*, [2017] compared the effectiveness of the single-stage and two-stage QZS nonlinear isolation systems and showed that the latter can exhibit a larger unity isolation frequency band. Moreover, a TS-VIS with mechanical mechanisms [Wang and Zhou *et al.*, 2017], one for gravity wave detectors [Matichard *et al.*, 2015] and active/hybrid ones [Xie *et al.*, 2019] have been studied. Floating raft vibration isolation structures have also been developed based on TS-VIS for reducing radiated noise of submarines [Lei *et al.*, 2018].

To further enhance the isolation performance, a recently developed passive device, the inerter, can be used [Smith, 2002]. The inerters have been realized in various ways using rack-pinion mechanisms, hydraulic fluid through a helical channel, or ball-screw mechanisms [Alujević *et al.*, 2018]. It was found that the addition of inerter can effectively improve the performance of isolators [He *et al.*, 2021; Morales, 2022; Wang *et. al.*, 2022; Dong *et al.*, 2021] or absorbers [Zhao *et al.*, 2021; Zhang *et al.*, 2020]. Wang *et. al.*, [2018] proposed eight different configurations of single-stage inerter-based linear isolators and assessed their isolation effectiveness by using response displacement and force transmissibility. The optimal parameters of structural design are obtained. Single-stage vibration isolators and tuned-mass-damper-inerter (TMDI) with geometrically nonlinear inerters have also been developed, demonstrating possible further enhancement on the vibration suppression compared to the structures with linear inerter, especially for the low-frequency vibration [Dai *et al.*, 2022a; Shi *et al.*, 2022; Liu *et al.*, 2022]. However, there are very few investigations on adding the inerter to TS-VIS [Yang *et al.*, 2019]. The use of geometrically nonlinear inerters in a TS-VIS has not been explored for enhancing vibration isolation performance [Yang *et al.*, 2017], despite being potentially applicable to typical engineering systems such as floating raft isolation structure.

In this research, a nonlinear inerter-based TS-VIS is proposed. After obtaining the responses of the TS-VIS, the transmissibility and power flow indicators are used for performance assessment and to reveal the vibration transmission mechanisms [Wang *et al.*, 2019; Zhao *et al.*, 2018]. The vibration power flow takes both force and velocity into account and makes a good performance index to quantify the vibration transmission [Goyder and White, 1980]. This method has been developed and used as an effective analysis tool in the investigation of linear systems [Renno *et al.*, 2019; Zhu *et al.*, 2021] and nonlinear systems such as vibration absorbers [Shi *et al.*, 2022], floating raft vibration isolation system and ship propulsion shafting system [Dai *et al.*, 2022a]. Recently, the power flow indices have been employed as fault diagnosis indicators in rotating machinery. Different severity of rub-impact faults can be detected by analysing the instantaneous or time-averaged energy transmission between the rotor and stator [Zhang *et al.*, 2023].

For the rest of the paper, a TS-VIS with nonlinear inerters is firstly presented in Section 2. In Section 3, the solution process of system responses is illustrated and the measures of evaluating the performance of the nonlinear isolator are defined. The effectiveness of the nonlinear TS-VIS is examined and discussed in Section 4, followed by conclusions.

2. Modelling of the Nonlinear Inerter-based TS-VIS

The TS-VIS with geometrically nonlinear inerters is shown in Figure 1(a). The upper stage comprises a harmonically excited machine of mass m_1, a vertical spring k_1, a vertical damper c_1, a vertical inerter of inertance b_1 and two identical lateral inerters b_2. The lower stage has a mass m_2, a vertical spring k_2, a vertical damper c_2, a vertical inerter b_3 and two identical lateral inerters b_4. The frequency and amplitude of the excitation force applied to m_1 are f_0 and ω, respectively. In the equilibrium state, the lateral inerters b_2 and b_4 are horizontal. The distance of two terminals of the lateral inerters when orientated horizontal is l.

Figure 1(b) shows the system with masses m_1 and m_2 having displacements x_1 and x_2, respectively. Fig. 2(c) and (d) plots force directions of two pairs of lateral inerters, respectively. The terminals O_1 and O_2 are attached to m_1 and m_2, respectively, θ_1 and θ_2 are the angles between AO_1 and AB and between CO_2 and CD with $\sin\theta_1 = (x_1 - x_2)/\sqrt{l^2 + (x_1 - x_2)^2}$ and $\sin\theta_2 = x_2/\sqrt{l^2 + x_2^2}$.

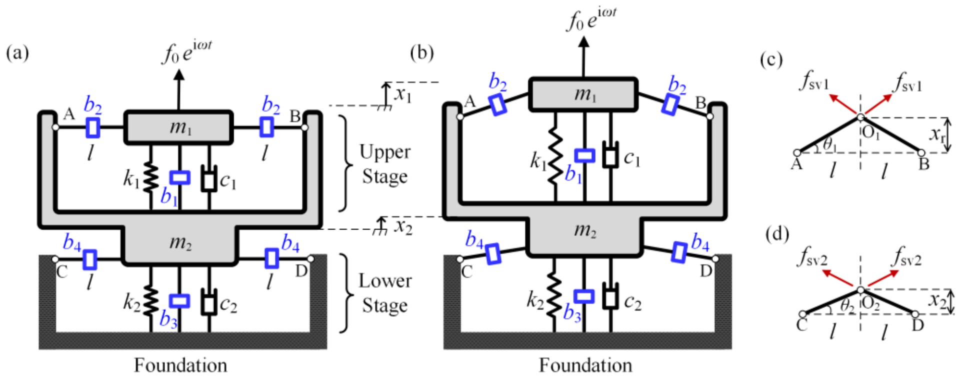

Figure 1. Schematics of (a) the proposed nonlinear TS-VIS at equilibrium state, (b) the proposed TS-VIS under deformation, (c) force analysis in the upper stage and (d) force analysis in the lower stage.

The governing equations of the nonlinear inerter-based TS-VIS are:

$$m_1\ddot{x}_1 + b_1\ddot{x}_r + c_1\dot{x}_r + k_1 x_r + f_{s1}\left(x_r, \dot{x}_r, \ddot{x}_r\right) = f_0 e^{i\omega t}, \quad (1)$$

$$\left(m_2 + b_3\right)\ddot{x}_2 - b_1\ddot{x}_r - c_1\dot{x}_r - k_1 x_r - f_{s1}\left(x_r, \dot{x}_r, \ddot{x}_r\right) + f_{s2}\left(x_2, \dot{x}_2, \ddot{x}_2\right) + c_2\dot{x}_2 + k_2 x_2 = 0, \quad (2)$$

where $x_r = x_1 - x_2$, $\dot{x}_r = \dot{x}_1 - \dot{x}_2$, $\ddot{x}_r = \ddot{x}_1 - \ddot{x}_2$ and $f_{s1}\left(x_r, \dot{x}_r, \ddot{x}_r\right)$ and $f_{s2}\left(x_2, \dot{x}_2, \ddot{x}_2\right)$ are the nonlinear forces generated by the lateral inerters in the two stages. From Fig. 1(c) and (d), the relative velocity between two terminals of the lateral inerter b_2 and b_4 can be expressed as $v_1 = \dot{x}_r \sin\theta_1$ and $v_2 = \dot{x}_2 \sin\theta_2$, respectively. Then the inerter forces f_{sv1} and f_{sv2} of inerters b_2 and b_4 can be determined as $f_{sv1} = b_2\left(\mathrm{d}v_1/\mathrm{d}t\right)$ and $f_{sv2} = b_4\left(\mathrm{d}v_2/\mathrm{d}t\right)$, respectively. Considering the symmetry of the structure, the total forces applied on two masses will be vertical and expressed as [Yang *et al.*, 2019]:

$$f_{s1}\left(x_r, \dot{x}_r, \ddot{x}_r\right) = 2 f_{sv1}\sin\theta_1 = 2b_2\left(\frac{x_r^2\ddot{x}_r}{l^2 + x_r^2} + \frac{l^2 x_r \dot{x}_r^2}{\left(l^2 + x_r^2\right)^2}\right), \quad (3)$$

$$f_{s2}\left(x_2, \dot{x}_2, \ddot{x}_2\right) = 2 f_{sv2}\sin\theta_2 = 2b_4\left(\frac{x_2^2\ddot{x}_2}{l^2 + x_2^2} + \frac{l^2 x_2 \dot{x}_2^2}{\left(l^2 + x_2^2\right)^2}\right). \quad (4)$$

The Eqs. (1) and (2) can be organized as:

$$\begin{bmatrix} m_1 + b_1 & -b_1 \\ -b_1 & m_2 + b_3 + b_1 \end{bmatrix}\begin{Bmatrix} \ddot{x}_1 \\ \ddot{x}_2 \end{Bmatrix} + \begin{bmatrix} k_1 & -k_1 \\ -k_1 & k_2 + k_1 \end{bmatrix}\begin{Bmatrix} x_1 \\ x_2 \end{Bmatrix} + \begin{bmatrix} c_1 & -c_1 \\ -c_1 & c_2 + c_1 \end{bmatrix}\begin{Bmatrix} \dot{x}_1 \\ \dot{x}_2 \end{Bmatrix}$$
$$+\begin{Bmatrix} f_{s1}\left(x_r, \dot{x}_r, \ddot{x}_r\right) \\ -f_{s1}\left(\ddot{x}_r, \dot{x}_r, x_r\right) + f_{s2}\left(x_2, \dot{x}_2, \ddot{x}_2\right) \end{Bmatrix} = \begin{Bmatrix} f_0 e^{i\omega t} \\ 0 \end{Bmatrix}. \quad (5)$$

here parameters are defined as:

$$\omega_1 = \sqrt{\frac{k_1}{m_1}},\quad \omega_2 = \sqrt{\frac{k_2}{m_2}},\quad \mu = \frac{m_2}{m_1},\quad \gamma = \frac{\omega_2}{\omega_1},\quad \zeta_1 = \frac{c_1}{2m_1\omega_1},\quad \zeta_2 = \frac{c_2}{2m_2\omega_2},\quad F_0 = \frac{f_0}{lk_1},$$

$$\Omega = \frac{\omega}{\omega_1},\quad \lambda_1 = \frac{b_1}{m_1},\quad \lambda_2 = \frac{b_2}{m_1},\quad \lambda_3 = \frac{b_3}{m_1},\quad \lambda_4 = \frac{b_4}{m_1},\quad X_1 = \frac{x_1}{l},\quad X_2 = \frac{x_2}{l},\quad X_\mathrm{r} = \frac{x_\mathrm{r}}{l},$$

$$\tau = \omega_1 t, \tag{6}$$

where ω_1 and ω_2 represent linearized resonant frequencies of subsystems in the upper and lower stages without inerters, respectively, μ and γ are the mass and natural frequency ratios, respectively, ζ_1 and ζ_2 are the damping coefficients, F_0 is the dimensionless excitation amplitude, Ω is dimensionless excitation frequency, λ_1, λ_2, λ_3 and λ_4 are the inertance ratios of the corresponding inerters, X_1, X_2 and X_r are the dimensionless displacements and the relative displacement of the masses, and τ is the dimensionless time. The governing equation is then transformed to a dimensionless form:

$$\begin{bmatrix} 1+\lambda_1 & -\lambda_1 \\ -\lambda_1 & \mu+\lambda_3+\lambda_1 \end{bmatrix} \begin{Bmatrix} X_1'' \\ X_2'' \end{Bmatrix} + \begin{bmatrix} 1 & -1 \\ -1 & \mu\gamma^2+1 \end{bmatrix} \begin{Bmatrix} X_1 \\ X_2 \end{Bmatrix} + \begin{bmatrix} 2\zeta_1 & -2\zeta_1 \\ -2\zeta_1 & 2\mu\gamma\zeta_2+2\zeta_1 \end{bmatrix} \begin{Bmatrix} X_1' \\ X_2' \end{Bmatrix} + \begin{Bmatrix} F_{\mathrm{s}1}\left(X_\mathrm{r}, X_\mathrm{r}', X_\mathrm{r}''\right) \\ -F_{\mathrm{s}1}\left(X_\mathrm{r}, X_\mathrm{r}', X_\mathrm{r}''\right) + F_{\mathrm{s}2}\left(X_2, X_2', X_2''\right) \end{Bmatrix} = \begin{Bmatrix} F_0 \mathrm{e}^{\mathrm{i}\Omega\tau} \\ 0 \end{Bmatrix}, \tag{7}$$

where

$$F_{\mathrm{s}1}\left(X_\mathrm{r}, X_\mathrm{r}', X_\mathrm{r}''\right) = 2\lambda_2 \left(\frac{X_\mathrm{r}^2 X_\mathrm{r}''}{1+X_\mathrm{r}^2} + \frac{X_\mathrm{r} X_\mathrm{r}'^2}{\left(1+X_\mathrm{r}^2\right)^2} \right), \tag{8}$$

$$F_{\mathrm{s}2}\left(X_2, X_2', X_2''\right) = 2\lambda_4 \left(\frac{X_2^2 X_2''}{1+X_2^2} + \frac{X_2 X_2'^2}{\left(1+X_2^2\right)^2} \right). \tag{9}$$

3. Dynamic Responses and Performance Indices

3.1. *Response analysis*

To solve the governing equation (7), the analytical and alternating-frequency-time (AFT) harmonic balance methods (HBM) are applied. Moreover, a numerical Runge-Kutta (RK) Dormand-Prince method with variable step size is also applied for validation. When using analytical HBM, the relative responses X_{r}, $X_{\mathrm{r}}^{'}$ and $X_{\mathrm{r}}^{''}$ of two masses as well as the responses X_2, $X_2^{'}$ and $X_2^{''}$ of the mass in the lower stage are approximated by

$$X_{\mathrm{r}} = H_1\cos\left(\Omega\tau+\alpha\right), X_2 = H_2\cos\left(\Omega\tau+\beta\right), \tag{10}$$

$$X_{\mathrm{r}}^{'} = -H_1\Omega\sin\left(\Omega\tau+\alpha\right), X_2^{'} = -H_2\Omega\sin\left(\Omega\tau+\beta\right) \quad , \tag{11}$$

$$X_{\mathrm{r}}^{''} = -H_1\Omega^2\cos\left(\Omega\tau+\alpha\right), X_2^{''} = -H_2\Omega^2\cos\left(\Omega\tau+\beta\right) \quad , \tag{12}$$

respectively, where H_1 and H_2 are the response amplitudes while α and β are the phase angles. By substituting Eqs. (10-12) into Eqs. (8) and (9), the nonlinear forces F_{s1} and F_{s2} can be approximated by Taylor expansion:

$$F_{\mathrm{s1}}\left(X_{\mathrm{r}}, X_{\mathrm{r}}^{'}, X_{\mathrm{r}}^{''}\right) \approx -\frac{\lambda_2\Omega^2H_1^3\left(H_1^2+2\right)}{2}\cos\left(\Omega\tau+\alpha\right), \tag{13}$$

$$F_{\mathrm{s2}}\left(X_2, X_2^{'}, X_2^{''}\right) \approx -\frac{\lambda_4\Omega^2H_2^3\left(H_2^2+2\right)}{2}\cos\left(\Omega\tau+\beta\right). \tag{14}$$

By substituting Eqs. (10-14) into Eq. (7), we have the following algebraic equations by using HBM:

$$\begin{aligned}&-2H_1\Omega\zeta_1\sin\alpha + H_1\left\{1-2\lambda_2\frac{\Omega^2H_1^2}{4}\left(H_1^2+2\right)\right\}\cos\alpha+\Omega^2\lambda_1H_2\cos\beta - \\ &\Omega^2\left(1+\lambda_1\right)\left(H_1\cos\alpha+H_2\cos\beta\right)=F_0\end{aligned}, \tag{15a}$$

$$\begin{aligned}&H_1\left\{2\lambda_2\frac{\Omega^2H_1^2}{4}\left(H_1^2+2\right)-1\right\}\sin\alpha-2\Omega\zeta_1H_1\cos\alpha+\Omega^2\left(1+\lambda_1\right)\left(H_1\sin\alpha+H_2\sin\beta\right)\\ &-\Omega^2\lambda_1H_2\sin\beta=0\end{aligned}, \tag{15b}$$

$$\begin{aligned}&2\Omega\zeta_1H_1\sin\alpha-2H_2\Omega\mu\gamma\zeta_2\sin\beta+\mu\gamma^2H_2\cos\beta+\\ &H_1\left\{2\lambda_2\frac{\Omega^2H_1^2}{4}\left(H_1^2+2\right)+\lambda_1\Omega^2-1\right\}\cos\alpha-\Omega^2H_2\left\{2\lambda_4\frac{H_2^2}{4}\left(H_2^2+2\right)-\mu-\lambda_3\right\}\cos\beta=0\end{aligned}, \tag{15c}$$

$$\begin{aligned}&2\Omega\zeta_1H_1\cos\alpha-2H_2\Omega\mu\gamma\zeta_2\cos\beta+H_1\left\{1-2\lambda_2\frac{\Omega^2H_1^2}{4}\left(H_1^2+2\right)-\lambda_1\Omega^2\right\}\sin\alpha+\\ &\left\{\Omega^2\left(\mu+\lambda_3\right)-\mu\gamma^2+2\lambda_4\frac{\Omega^2H_2^2}{4}\left(H_2^2+2\right)\right\}H_2\sin\beta=0\end{aligned}. \tag{15d}$$

By using the Newton-Raphson method to solve Eq. (15), we can determine solutions of H_1, H_2, α and β for further performance evaluation of the nonlinear isolator.

When the displacements of the masses become large, the inertial nonlinearity becomes stronger and the use of analytical HBM of relative low orders may lead to reduced accuracy of the results. To improve the approximation accuracy of the system response, a higher order of harmonic terms is needed. However, due to the complexity of function of nonlinear force, it is challenging to obtain the high order terms of nonlinear forces analytically. Therefore, in determination of the approximated nonlinear force expression, a specific form of HBM, namely HBM-AFT (alternating frequency time) scheme is used here to obtain the Fourier coefficients of nonlinear forces numerically. In practice, assuming that the responses of two masses can be expressed by Q -order Fourier series:

$$X_1 = \sum_{q=0}^{Q} \tilde{J}_{(1,q)} \exp(\mathrm{i}q\Omega\tau), \qquad X_2 = \sum_{q=0}^{Q} \tilde{J}_{(2,q)} \exp(\mathrm{i}q\Omega\tau), \qquad \text{(16a, 16b)}$$

where q is an integer within the range of $[0, Q]$, $\tilde{J}_{(1,q)}$ and $\tilde{J}_{(2,q)}$ are the approximated q -th order complex Fourier coefficients of the responses. The nonlinear forces F_{s1} and F_{s2} of the inerter-configuration can be also approximated as

$$F_{\mathrm{s1}}\left(X_{\mathrm{r}}, X_{\mathrm{r}}^{'}, X_{\mathrm{r}}^{''}\right) = \sum_{q=0}^{Q} \tilde{S}_{(1,q)} \exp(\mathrm{i}q\Omega\tau), \qquad \text{(17a)}$$

$$F_{\mathrm{s2}}\left(X_2, X_2^{'}, X_2^{''}\right) = \sum_{q=0}^{Q} \tilde{S}_{(2,q)} \exp(\mathrm{i}q\Omega\tau), \qquad \text{(17b)}$$

where $\tilde{S}_{(1,q)}$ and $\tilde{S}_{(2,q)}$ are the approximated q -th order complex Fourier coefficients. Here the AFT technique is implemented to obtain the coefficients $\tilde{S}_{(1,q)}$ and $\tilde{S}_{(2,q)}$ of the nonlinear forces. The approximated displacement responses in Eq. (16), and velocity responses and acceleration responses obtained by the differentiation of Eq. (16), are substituted into Eq. (17), to obtain the time histories of the nonlinear forces. Then the time-domain expression of nonlinear forces can be Fourier transformed into frequency domain and the coefficients $\tilde{S}_{(1,q)}$ and $\tilde{S}_{(2,q)}$ can be determined.

The approximated responses and nonlinear forces in Eqs. (16) and (17) can be substituted into the governing equation (7). Based on HBM, the terms with the same order are balanced. For the q -th order harmonic balance, we have [Dai et al., 2022b]

$$\left(-\left(q\Omega\right)^{2}\begin{bmatrix}1+\lambda_1 & -\lambda_1\\ -\lambda_1 & \mu+\lambda_3+\lambda_1\end{bmatrix}+\begin{bmatrix}1 & -1\\ -1 & \mu\gamma^{2}+1\end{bmatrix}+\mathrm{i}\left(q\Omega\right)\begin{bmatrix}2\zeta_1 & -2\zeta_1\\ -2\zeta_1 & 2\mu\gamma\zeta_2+2\zeta_1\end{bmatrix}\right)\begin{Bmatrix}\tilde{J}_{(1,q)}\\ \tilde{J}_{(2,q)}\end{Bmatrix}=\begin{Bmatrix}F_0-\tilde{S}_{(1,q)}\\ \tilde{S}_{(1,q)}-\tilde{S}_{(2,q)}\end{Bmatrix}. \tag{18}$$

Therefore, $2(2Q+1)$ algebraic equations are obtained. Here the Newton-Rapson method is used for solving those equations. In order to track the possible branches of solution, the numerical continuation method is applied to calculate the solutions [Colaïtis and Batailly, 2021; Dai *et al.*, 2020].

3.2. *Isolation performance indicators*

To assess the performance of TS-VIS, the force transmissibility is used as an index to evaluate the level of vibration transmission. The force transmissibility is defined as the maximum magnitude of the transmitted forces to that of the input force. The force transmissibilities to the lower stage and to the ground are defined as

$$TR_{\mathrm{i}}=\frac{\left|F_{\mathrm{ti}}\right|_{\max}}{F_0}, \qquad TR_{\mathrm{f}}=\frac{\left|F_{\mathrm{tf}}\right|_{\max}}{F_0}, \tag{19}$$

respectively, where F_{ti} and F_{tf} are the corresponding transmitted forces. In this paper, the vibration generated by the machine m_1 is transmitted via inerters b_1, b_2, spring k_1 and damper c_1 to the lower stage m_2. The vibration of lower stage is transmitted via inerters b_3, b_4, spring k_2 and damper c_2 to the ground. Therefore, the total transmitted force to the lower stage and to the ground can be obtained as the total vertical transmitted force between m_1 and m_2 and between m_2 and ground, respectively, which can be derived as

$$F_{\mathrm{ti}}=F_{\mathrm{s1}}\left(X_{\mathrm{r}},X_{\mathrm{r}}^{'},X_{\mathrm{r}}^{''}\right)+X_{\mathrm{r}}+2\zeta_1X_{\mathrm{r}}^{'}+\lambda_1X_{\mathrm{r}}^{''}=2\lambda_2\left(\frac{X_{\mathrm{r}}^{2}X_{\mathrm{r}}^{''}}{1+X_{\mathrm{r}}^{2}}+\frac{X_{\mathrm{r}}X_{\mathrm{r}}^{'2}}{\left(1+X_{\mathrm{r}}^{2}\right)^{2}}\right)+X_{\mathrm{r}}+2\zeta_1X_{\mathrm{r}}^{'}+\lambda_1X_{\mathrm{r}}^{''}, \tag{20}$$

$$F_{\mathrm{tf}}=F_{\mathrm{s2}}\left(X_2,X_2^{'},X_2^{''}\right)+\mu\gamma^{2}X_2+2\mu\gamma\zeta_2X_2^{'}+\lambda_3X_2^{''}=2\lambda_4\left(\frac{X_2^{2}X_2^{''}}{1+X_2^{2}}+\frac{X_2X_2^{'2}}{\left(1+X_2^{2}\right)^{2}}\right)+\mu\gamma^{2}X_2+2\mu\gamma\zeta_2X_2^{'}+\lambda_3X_2^{''}, \tag{21}$$

respectively. By the substitution of Eqs. (10-14) into Eq. (20) and (21), the analytically approximated transmitted forces F_{ti} and F_{tf} are

$$F_{\mathrm{ti}} \approx H_1\left(-\frac{\lambda_2\Omega^2 H_1^2\left(H_1^2+2\right)}{2}-\lambda_1\Omega^2+1\right)\cos\left(\Omega\tau+\alpha\right)-2\Omega\zeta_1 H_1\sin\left(\Omega\tau+\alpha\right), \quad (22)$$

$$F_{\mathrm{tf}} \approx H_2\left(\mu\gamma^2-\frac{\lambda_4\Omega^2 H_2^2\left(H_2^2+2\right)}{2}-\lambda_3\Omega^2\right)\cos\left(\Omega\tau+\beta\right)-2\Omega\mu\gamma\zeta_2 H_2\sin\left(\Omega\tau+\beta\right). \quad (23)$$

Therefore, the corresponding force transmissibilities are approximated as

$$TR_{\mathrm{i}}=\frac{\left|F_{\mathrm{ti}}\right|_{\max}}{F_0}\approx\frac{H_1\sqrt{\left(-\frac{\lambda_2\Omega^2 H_1^2\left(H_1^2+2\right)}{2}-\lambda_1\Omega^2+1\right)^2+\left(2\zeta_1\Omega\right)^2}}{F_0}, \quad (24)$$

$$TR_{\mathrm{f}}=\frac{\left|F_{\mathrm{tf}}\right|_{\max}}{F_0}\approx\frac{H_2\sqrt{\left(-\frac{\lambda_4\Omega^2 H_2^2\left(H_2^2+2\right)}{2}-\lambda_3\Omega^2+\mu\gamma^2\right)^2+\left(2\mu\gamma\zeta_2\Omega\right)^2}}{F_0}. \quad (25)$$

Equations (24) and (25) show that for the linear undamped isolation system with $\lambda_2=\lambda_4=\zeta_1=\zeta_2=0$, the force transmissibilities TR_{i} and TR_{f} are zero, at the excitation frequencies of

$$\Omega=\Omega_1=\sqrt{1/\lambda_1} \qquad \Omega=\Omega_2=\sqrt{\mu\gamma^2/\lambda_3}, \quad (26\text{a}, 26\text{b})$$

respectively. For the current nonlinear TS-VIS with weak damping, TR_{i} and TR_{f} will take quasi-zero values at Ω_1 or Ω_2. It is noted that the values of Ω_1 and Ω_2 for ultra-low force transmission can be tuned by changing the inertance ratios λ_1 and λ_3. This characteristic demonstrates that by designing inertances of vertical and lateral inerters, the force transmission can be significantly suppressed.

The instantaneous input vibrational power is defined as [Dai *et al.*, 2022c]:

$$P_{\mathrm{in}}=\mathrm{R}\left\{F_0 e^{\mathrm{i}\Omega\tau}\right\}\mathrm{R}\left\{X_1^{'}\right\}=\mathrm{R}\left\{F_0 e^{\mathrm{i}\Omega\tau}\right\}\mathrm{R}\left\{\sum_{q=0}^{Q}\mathrm{i}q\Omega\tilde{J}_{(1,q)}\exp\left(\mathrm{i}q\Omega\tau\right)\right\}, \quad (27)$$

where $\mathrm{R}\{\}$ represents real part of the variable. The corresponding time-averaged input vibrational power is

$$\bar{P}_{\mathrm{in}}=\frac{1}{\tau_{\mathrm{p}}}\int_{\tau_0}^{\tau_0+\tau_{\mathrm{p}}}P_{\mathrm{in}}\mathrm{d}\tau=\frac{1}{\tau_{\mathrm{p}}}\mathrm{R}\int_{\tau_0}^{\tau_0+\tau_{\mathrm{p}}}\left\{F_0 e^{\mathrm{i}\Omega\tau}\right\}\mathrm{R}\left\{X_1^{'}\right\}\mathrm{d}\tau=\frac{1}{2}F_0\mathrm{R}\left\{\left(\mathrm{i}\Omega\tilde{J}_{(1,1)}\right)^*\right\}, \quad (28)$$

where τ_{p} is defined as an excitation cycle in the steady state, i.e., $2\pi/\Omega$, and ()* denotes the complex conjugate of the variable. Using approximate expressions of the velocity shown by Eq. (11), we have the approximated time-averaged input vibrational power

$$\bar{P}_{\mathrm{in}} = \frac{1}{\tau_{\mathrm{p}}}\int_{\tau_0}^{\tau_0+\tau_{\mathrm{p}}} \left(X_1' F_0 \cos\Omega\tau \right) \mathrm{d}\tau \approx -\frac{F_0\Omega}{2}\left(H_1\cos\alpha + H_2\cos\beta \right). \tag{29}$$

The power transmission to the lower stage is dissipated by c_2, therefore, we can define the instantaneous power transmission P_{t} and time-averaged power transmission $\bar{P}_{\mathrm{t}}$ expressed as

$$P_{\mathrm{t}} = 2\zeta_2\mu\gamma(\mathrm{R}\{X_2'\})^2 = 2\zeta_2\mu\gamma(\mathrm{R}\{\sum_{q=0}^{Q}\mathrm{i}q\Omega\tilde{J}_{(2,q)}\exp\left(\mathrm{i}q\Omega\tau\right)\})^2, \tag{30}$$

$$\begin{aligned}\bar{P}_{\mathrm{t}} &= \frac{1}{\tau_{\mathrm{p}}}\int_{\tau_0}^{\tau_0+\tau_{\mathrm{p}}} 2\zeta_2\mu\gamma(\mathrm{R}\{X_2'\})^2\,\mathrm{d}\tau = \frac{1}{\tau_{\mathrm{p}}}\int_{\tau_0}^{\tau_0+\tau_{\mathrm{p}}} 2\zeta_2\mu\gamma(\mathrm{R}\{\sum_{q=0}^{Q}\mathrm{i}q\Omega\tilde{J}_{(2,q)}\exp\left(\mathrm{i}q\Omega\tau\right)\})^2\,\mathrm{d}\tau \\ &= \frac{1}{2}\mathrm{R}\left\{\left(\sum_{q=0}^{Q}\mathrm{i}q\Omega\tilde{J}_{(2,q)}\right)^{*}\left(2\zeta_2\mu\gamma\sum_{q=0}^{Q}\mathrm{i}q\Omega\tilde{J}_{(2,q)}\right)\right\} = \zeta_2\mu\gamma\left|\sum_{q=0}^{Q}\mathrm{i}q\Omega\tilde{J}_{(2,q)}\right|^2\end{aligned}, \tag{31}$$

respectively. By a substitution of Eqs. (10)-(12) to Eq. (31), the analytically approximated transmitted power to the lower stage is expressed as

$$\bar{P}_{\mathrm{t}} = \frac{1}{\tau_{\mathrm{p}}}\int_{\tau_0}^{\tau_0+\tau_{\mathrm{p}}} 2\zeta_2\mu\gamma\Omega^2 H_2^2 \sin^2\left(\Omega\tau+\beta\right)\mathrm{d}\tau \approx \zeta_2\mu\gamma\Omega^2 H_2^2. \tag{32}$$

The power transmission ratio is therefore obtained using Eqs. (28) and (31):

$$R_{\mathrm{t}} = \frac{\bar{P}_{\mathrm{t}}}{\bar{P}_{\mathrm{in}}} = \frac{F_0\mathrm{R}\left\{\left(\mathrm{i}\Omega\tilde{J}_{(1,1)}\right)^{*}\right\}}{2\zeta_2\mu\gamma\left|\sum_{q=0}^{Q}\mathrm{i}q\Omega\tilde{J}_{(2,q)}\right|^2}, \tag{33}$$

and the corresponding approximated power transmission ratio is

$$R_{\mathrm{t}} = \frac{\bar{P}_{\mathrm{t}}}{\bar{P}_{\mathrm{in}}} \approx \frac{2\zeta_2\mu\gamma\Omega H_2^2}{-F_0\left(H_1\cos\alpha + H_2\cos\beta\right)}. \tag{34}$$

4. Results and Discussion

This section presents the performance assessment on the TS-VIS. In Fig. 2, the response amplitudes of two masses obtained from analytical HBM, HBM-AFT with harmonic order $Q = 4$ and numerical integration RK methods are compared. The inertance ratios of the inerters are set as λ_1 = 0.5, λ_2 = 10, λ_3 = 1 and λ_4 = 10, respectively. A linear system without using inerters is also considered with the results presented. The other parameters are fixed at $F_0 = 0.004, \mu = \lambda = \gamma = 1, \zeta_1 = \zeta_2 = 0.01$ throughout the paper.

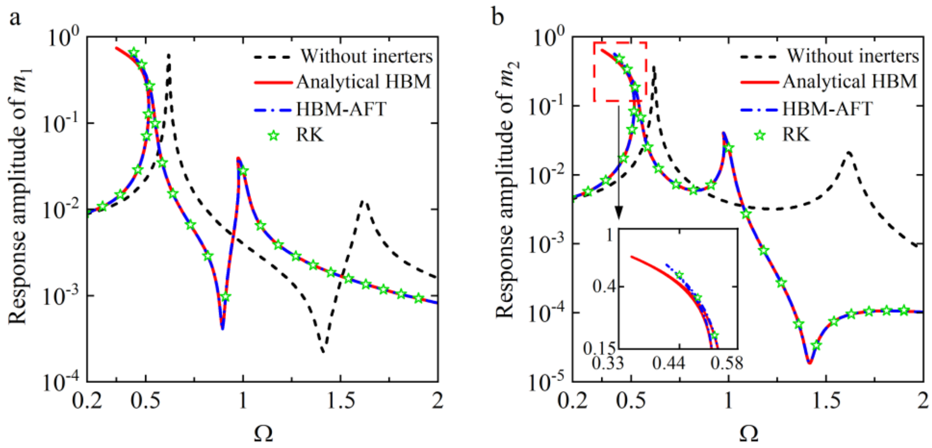

Figure 2. Comparison of the response amplitudes of the masses (a) m_1 and (b) m_2, obtained by different methods. The dashed line denotes the linear case without inerters. Solid line: analytical HBM. Dash-dotted line: HBM-AFT. Stars: RK results.

Figure 2 shows that in each response curve, there are two resonant peaks, with both bending left for the nonlinear cases. This behaviour of the proposed isolator is caused by the geometric inertial nonlinearity of the inerters in the upper and lower stages. The figure shows that the analytical HBM and HBM-AFT results agree well. Near the first peak of the curves ($\Omega \approx 0.5$), discrepancies between the results from different methods become noticeable. A comparison of the results obtained from the RK method shown in the enlarged plot in Fig. 2(b) shows that the HBM-AFT with harmonic order of $Q = 4$ can provide a good approximation of the responses even when the nonlinear isolator undergoes large deflection. Noting that choosing a higher order of Q may further increase the accuracy of response approximation, but the computation cost will also increase. Therefore, by a balanced consideration of efficiency and accuracy, the value of Q is set as 4 throughout the paper. In view of this, the results obtained from HBM-AFT and RK methods are used and shown in the rest of this paper for the performance evaluations of the proposed isolator.

In Figs. 3 and 4, the influence of the inerters in the upper stage of the TS-VIS on the effectiveness of the isolator is examined. In Fig. 3, four inertance ratios of the vertical inerter with λ_1 being 0.5, 0.8, 1 and 1.2 are considered while the lateral inerters λ_2 is fixed at 20. In Fig. 4, the inertance ratio λ_2 varies from 5 to 20 while λ_1 is set as 1. The inertance ratios in the lower stage are fixed at 0.

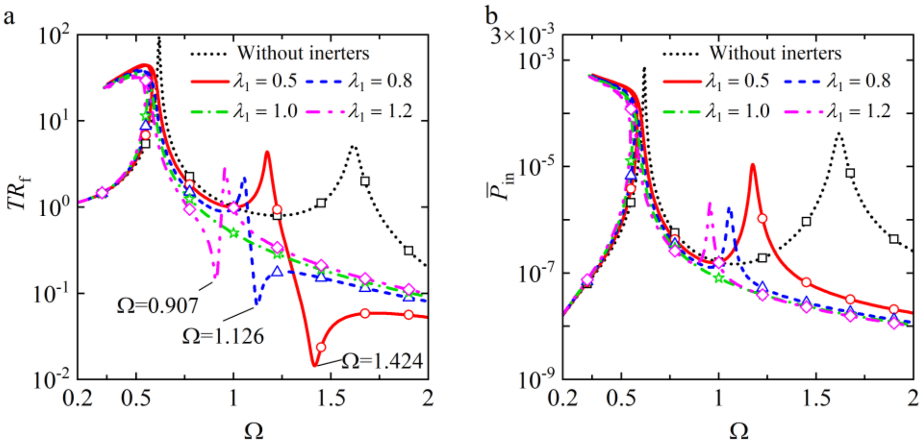

Figure 3. Variations of the (a) transmissibility and (b) input power under the influence of the inertance ratio λ_1 in the upper stage. The black dotted line denotes the non-inerter case result. Different lines are for the cases with λ_1 =0.5, 0.8, 1 and 1.2. The symbols denote RK results.

Figure 3(a) shows the inerters in upper stage can lead to left bending of the first peak and introduce an anti-resonance peak in force transmissibility curve. The anti-peak frequency can be approximated by using the analytical expressions of force transmissibilities shown by Eqs. (24) and (25). With the inertance λ_1 and λ_2 at specific values, the force transmissibility to the lower stage or to the ground can be tuned and effectively suppressed at designed frequency Ω. In particular, for undamped system with $\lambda_2 = 0$, the analytical predicted anti-peak frequency $\Omega_{\mathrm{anti}} = \sqrt{1/\lambda_1}$ being 0.913, 1.118 and 1.414 when $\lambda_1 = 1.2$, 0.8 and 0.5, respectively, agreeing well with the marked anti-peak frequencies 0.907, 1.126 and 1.424 in Fig. 3(a) determined by using HBM-AFT. This characteristic enables the placement of a notch in the force transmissibility curve at particular frequencies by setting a specific value of λ_1, desirable for low-frequency isolation of unbalanced machines operating at a low rotational speed.

Figure 3(a) also shows increasing the inertance λ_1 can shift resonance peaks to the left. It is shown that the second peak is decreased significantly by using inerters. Only one peak is noticeable in the dash-dotted line with λ_1 =1, showing a broad frequency band of effective isolation with TR_{f} being lower than unity. The reason is that the vertical inerter can generate an anti-resonance peak (i.e., a notch) in force transmissibility curve. The second peak of the corresponding TS-VIS without using inerters can be suppressed by introducing inerters and then setting the anti-peak frequency at the original second peak frequency. An increase in λ_1 can move both peaks of $\bar{P}_{\mathrm{in}}$ to the left with lower peak heights, as shown in Fig. 3(b). Moreover, only one peak is found in the curve with $\lambda_1 = 1$. It demonstrates that vibrational energy input can be reduced significantly by designing the value of the vertical inertance λ_1 in the upper stage.

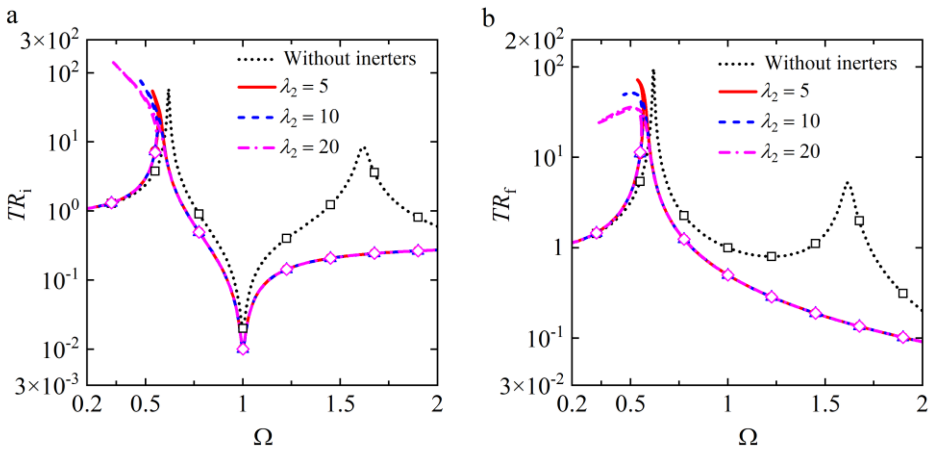

Figure 4. Variations of transmissibility (a) to lower stage and (b) to foundation under the influence of the inertance ratio λ_2 in the upper stage. The black dotted line denotes the non-inerter case result. Different lines denote the cases with λ_2 =5, 10 and 20. The symbols denote RK results.

Figure 4 depicts the variations of TR_i and TR_f under different lateral inertance λ_2. Comparing to the linear non-inerter TS-VIS case containing two well-separated peaks in the transmissibility curve, the force transmissibility of the proposed TS-VIS to the lower stage and that to the ground is lower in a wide frequency band, demonstrating a much better isolation performance. By changing λ_2 from 5 to 20, the first peak in TR_f curve extends further towards left with lower height. The results show that a larger λ_2 can enhance the low-frequency isolation.

In Figs. 5 and 6, the effects of the inerters in the lower stage on the performance of TS-VIS are investigated. The inertance ratios in the upper stage are set as 0. In Fig. 5, the inertance ratio λ_3 is varied from 0.2 to 1.2 while that of the lateral inerters λ_4 is fixed at 5. Fig. 5(a) shows that peaks in transmissibility TR_f curve shift towards left as λ_3 increases. An anti-resonance peak is found and the corresponding frequency depends on the values of λ_3 and λ_4, as predicted previously from the analytical derivation of force transmissibility in Eq. (25). For the undamped system with $\lambda_4 = 0$, the anti-peak frequency is $\Omega_{\text{anti}} = \sqrt{\mu\gamma^2 / \lambda_3}$. With λ_3 being 1.2 and 0.8, the analytically predicted anti-peak frequencies are 0.913 and 1.118, respectively, which are close to 0.910 and 1.120, determined by the HB-AFT and marked in Fig. 5(a). The results show that the anti-peak frequency of force transmissibility can be designed by adjusting inertance λ_3 based on the dominant low-frequency line spectrum of the working machinery to provide an ultra-low force transmission. Moreover, both peaks of force transmissibility are shifted further to the left when the inertance λ_3 increases. The height of the second peak is reduced when λ_3 changes from 0.2 to 0.5 but it increases when λ_3 changes from 0.5 to 1.2. At λ_3 = 0.5, only one noticeable peak is found in TR_f curve, yielding a much broader frequency band of unity force transmissibility compared to that of the linear non-inerter system. This characteristic can be also combined with the effect of the vertical inerter λ_1 in the upper stage of the system to provide enhanced isolation performance. Fig. 5(b) presents the power transmission ratio R_t to the lower stage of TS-VIS. As inertance λ_3 varies from 0.5 to 1.2, R_t starts to reduce when $\Omega > 0.75$.

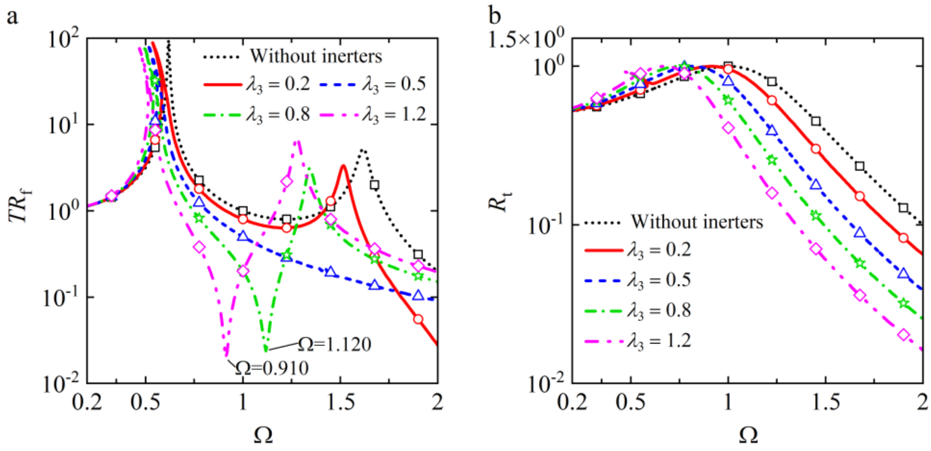

Figure 5. Changes of (a) TR_f and (b) R_t by varying the inertance ratio λ_3 of the lower stage. The black line denotes the non-inerter case result. The black dotted line denotes the non-inerter case result. Different lines are for λ_3 =0.2, 0.5, 0.8 and 1.2 cases. The symbols denote RK results.

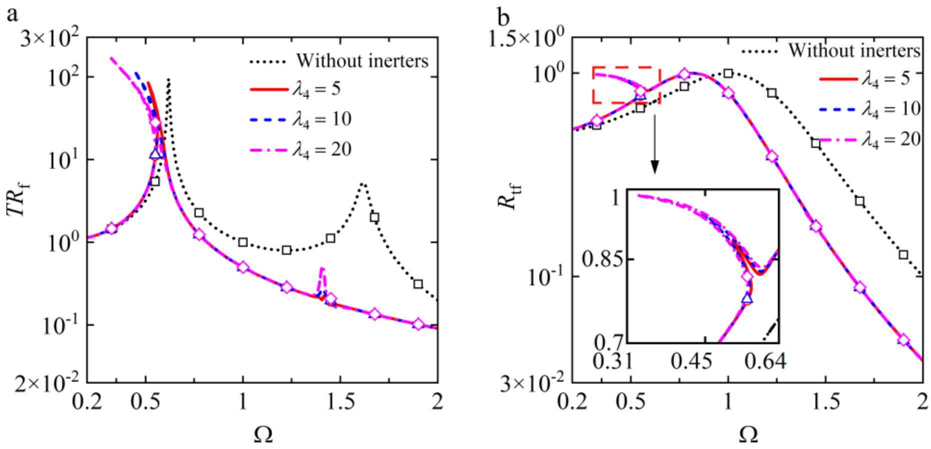

Figure 6. Variations of the (a) transmissibility and (b) energy transmission ratio under changes of the inertance ratio λ_4 in the lower stage. The black dotted line denotes the non-inerter case result. Different lines denote the cases with λ_4 = 5, 10 and 20. The symbols denote RK results.

In Fig. 6, the inertance ratio λ_4 of lateral inerters in the lower stage is changed from 5 to 10, and then to 20 while λ_3 of the vertical inerter is set as 0.5. Fig. 6(a) shows that a larger λ_4 will bend the first peak of TR_f to left. Fig. 6(b) shows that the lateral inertance λ_4 has little influence on the R_t when Ω is not in the first resonance region, shown by the merged curves of power transmission ratio in $\lambda_4 =$ 5, 10 and 20 cases. The reason is that the system exhibits significant geometric nonlinearity when the nonlinear isolator undergoes large deflection. From the enlarged plot in Fig. 6(b), the increase of the inertance λ_4 can lead to a higher power transmission ratio. Therefore, the value of λ_4 should be better controlled in a relatively low value to restrain the amount of the energy transferred to the lower base.

Here, the use of inerters in both stages is considered to seek further improvement on the performance. In Figs. 7 and 8, vibration transmission indicators of four different configurations of the inerter-based TS-VIS are compared. In configurations C1 and C2, the inerters are applied in the upper stage only and in the lower stage only, respectively. The parameters are selected as $\lambda_1 = 1$, $\lambda_2 = 5$, $\lambda_3 = \lambda_4 = 0$ and $\lambda_1 = \lambda_2 = 0$, $\lambda_3 = 0.5$, $\lambda_4 = 5$, represented by the solid(red) and dashed(blue) lines, respectively. In configurations C3 and C4, the inerters are used in both stages. The parameters are set as $\lambda_1 = 0.5$, $\lambda_2 = 5$, $\lambda_3 = 1$, $\lambda_4 = 5$ and $\lambda_1 = 2$, $\lambda_2 = 5$, $\lambda_3 = 1$, $\lambda_4 = 5$, denoted by the dash-dotted(green) and dash-dot-dot(pink) lines, respectively. The results for the corresponding linear TS-VIS without inerters (i.e., non-inerter case) are also added as black dotted line.

Figure 7(a) depicts that the curves of transmissibility in configurations C1 and C2 almost coincide with each other. It is shown that the inerters in the upper and lower stages share a similar effect on the force transmission. The values of TR_{f} for configurations C1 and C2 are much smaller than those of the corresponding linear non-inerter cases in the mid- and low- frequency ranges. For configurations C3 and C4, the value of TR_{f} is further reduced when $0.5 < \Omega < 1.5$, compared to the corresponding value associated with configurations C1 and C2. There is a local minimum in the curve of TR_{f}. It is also possible to design the corresponding frequency by adjusting the inertance ratios. It is demonstrated that a combined use of the inerters in upper and lower stages can suppress force transmission, especially for the low-frequency vibration isolation.

Figure 7(b) shows that the $\bar{P}_{\mathrm{t}}$ curve for configuration C1 has a similar trend, compared to that of configuration C4. However, the configuration C4 case demonstrates a better isolation performance than configuration C1 by further reducing the $\bar{P}_{\mathrm{t}}$ values in a wide frequency band. This beneficial characteristic originates from the combined use of inerters in upper and lower stages. For configuration C2, there is a peak shifting effect caused by the addition of the inerters, while in the configuration C3 case, an anti-peak is generated, which can be applied for achieving exceptional vibration isolation at the prescribed excitation frequency. The results demonstrate that the inertance values of inerters in both stages of the VIS should be designed simultaneously for enhanced vibration isolation performance.

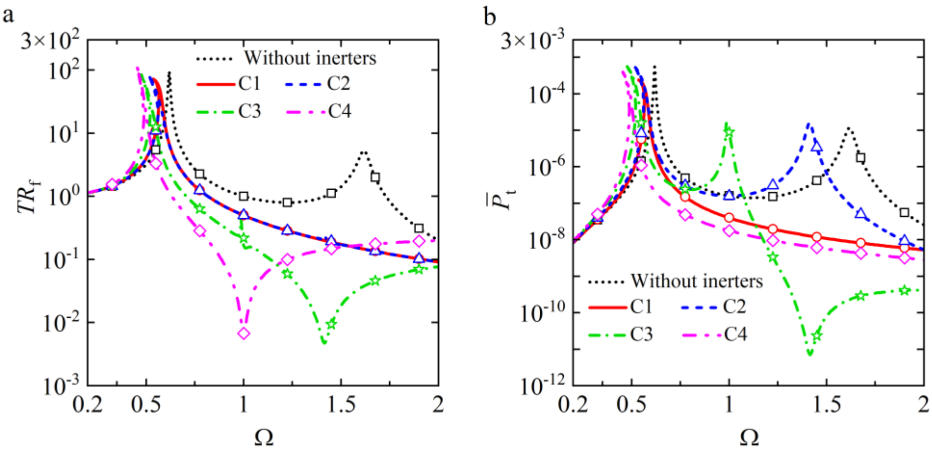

Figure 7. Influence of different configurations of the proposed nonlinear isolator on (a) transmissibility and (b) energy transmission. The black line denotes the non-inerter case result. Different lines denote four configurations, respectively. The symbols denote RK results.

Figure 8 further compares the time history of instantaneous transmitted force and instantaneous power flow at pre-described frequencies between four configurations of C1, C2, C3 and C4. A linear TS-VIS without using inerters is also shown for reference. Fig. 8(a) shows the instantaneous transmitted force to the ground in the steady state at $\Omega=1.4$, while Fig. 8(b) shows the instantaneous transmitted force F_{tf} to the ground at $\Omega=1.6$. It is found that the amplitude of transmitted force to ground is considerably reduced by using inerters. In addition, the value of transmitted force to the ground in configuration C3 is close to zero, suggesting an ultra-low force transmission to the ground. This phenomenon also indicates that the integration of nonlinear inerters in both stages can further enhance the effectiveness of vibration isolation. Fig. 8(c) shows the instantaneous input vibrational power into the system P_{in} and Fig. 8(d) depicts the instantaneous power transfer to the ground P_t. It is found that the use of inerters in two-stage vibration isolation system can largely decrease the amplitude of vibrational energy input and also suppress the amount of vibrational energy transfer to the ground. By a combined analysis of time-averaged power flow and instantaneous power flow indices, it can be summarized that the TS-VIS with nonlinear inerters embedded in two stages can provide a superior vibration isolation performance.

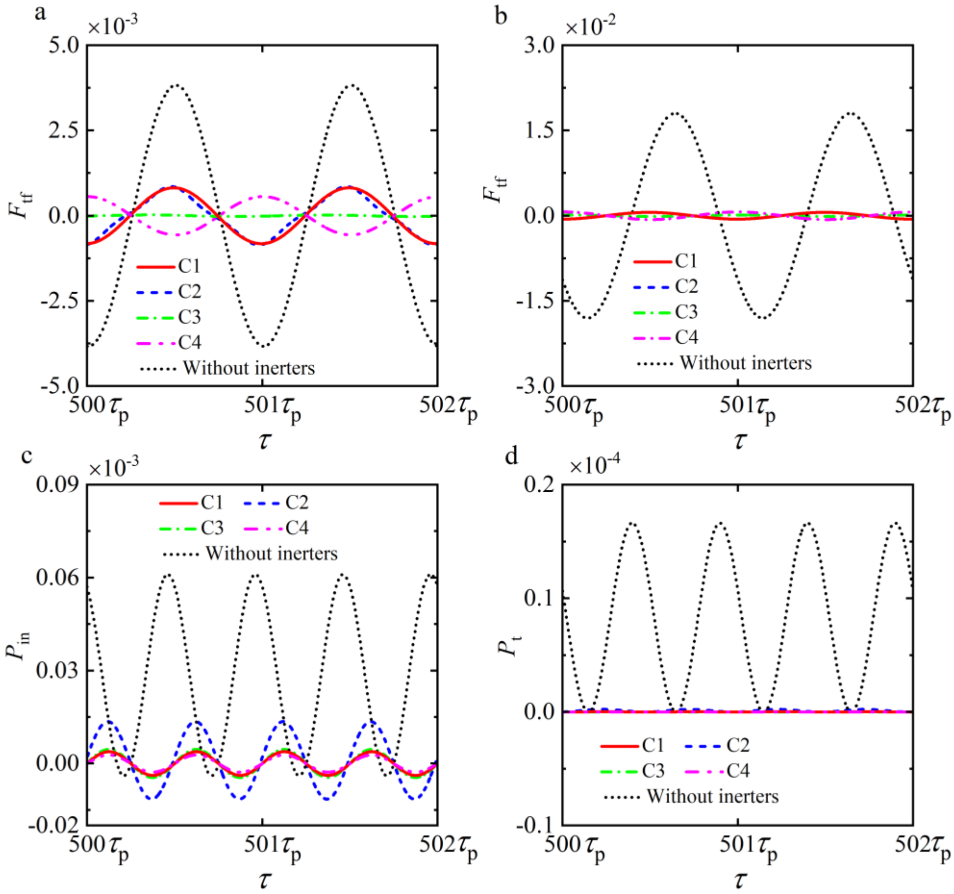

Figure 8. Time history of instantaneous (a) transmitted force F_{tf} to the ground at $\Omega=1.4$, (b) transmitted force F_{tf} to the ground at $\Omega=1.6$, (c) instantaneous input vibrational power P_{in} at $\Omega=1.6$ and (d) instantaneous transmitted power P_t to the ground at $\Omega=1.6$. The black line denotes the non-inerter case result. Different lines denote four configurations, respectively.

5. Conclusions

This research proposed a vibration isolator with geometric nonlinearity created by inerters and evaluated its performance. The system can be considered as a representative model of isolation system in engineering applications such as typical floating raft platform. The force and energy transmission indices were chosen to assess the isolation performance. It is demonstrated that the geometric nonlinearity of inerters can be exploited to yield a leftwards-bending characteristic in response curves. The inerters in the upper stage or lower stage can widen substantially the effective isolation band by shifting resonance peaks to the lower frequencies. The peak values of the force transmissibility can be suppressed by using the proposed inerter-based two-stage vibration isolator. An anti-resonance peak is generated in the force transmission curve and power transmission curve by using inerters such that vibration transmission is significantly attenuated at desired frequency. Moreover, analytical derivations and numerical simulations both demonstrate that the second peak in force transmissibility and energy transmission curves of the corresponding system without inerters can be suppressed by properly selecting the inertance ratios at analytically predicted values. The amount of input energy is reduced and the energy transmission ratio is decreased in a large frequency band. Enhanced performance of vibration isolation can be attained via the combined use and design of inerters in both stages of the isolator.

Acknowledgments

This work was supported by National Natural Science Foundation of China [Grant numbers 12202152, 12172185, 51839005], by the Zhejiang Provincial Natural Science Foundation of China [Grant number LY22A020006] and by the Ningbo Municipal Natural Science Foundation [Grant number 2022J174].

References

Alujević, N., Čakmak, D., Wolf, H. and Jokić, M. [2018] "Passive and active vibration isolation systems using inerter," *Journal of Sound and Vibration* **418**, 163-183.

Chen, D., Zi, H., Li, Y. and Li, X. [2021] "Low frequency ship vibration isolation using the band gap concept of sandwich plate-type elastic metastructures," *Ocean Engineering* **235**, 109460.

Colaïtis, Y., & Batailly, A. [2021] "The harmonic balance method with arc-length continuation in blade-tip/casing contact problems" *Journal of Sound and Vibration* **502**, 116070.

Dai, W., Yang, J. and Shi, B. [2020] "Vibration transmission and power flow in impact oscillators with linear and nonlinear constraints," *International Journal of Mechanical Sciences* **168**, 105234.

Dai, W. and Yang, J. [2021] "Vibration transmission and energy flow of impact oscillators with nonlinear motion constraints created by diamond-shaped linkage mechanism," *International Journal of Mechanical Sciences* **194**, 106212.

Dai, W., Shi, B., Yang, J., Zhu, X. and Li, T. [2022a] "Enhanced suppression of longitudinal vibration transmission in propulsion shaft system using nonlinear tuned mass damper inerter," *Journal of Vibration and Control*, 10775463221081183. Epub ahead of print 7 May 2022. DOI: 10.1177/10775463221081183.

Dai, W., Li, T. and Yang, J. [2022b] "Energy flow and performance of a nonlinear vibration isolator exploiting geometric nonlinearity by embedding springs in linkages," *Acta Mechanica* **233**, 1663-1687.

Dai, W., Yang, J., and Wiercigroch, M. [2022c] "Vibration energy flow transmission in systems with Coulomb friction," *International Journal of Mechanical Sciences* **214**, 106932.

Dong, Z., Chronopoulos, D., Yang, J. [2021] "Enhancement of wave damping for metamaterial beam structures with embedded inerter-based configurations," *Applied Acoustics* **178**, 108013.

Goyder, H.G.D. and White, R.G. [1980] "Vibrational power flow from machines into built-up structures, part I: Introduction and approximate analyses of beam and plate-like foundations," *Journal of Sound and Vibration* **68**, 59-75.

He, H., Li, Y., Jiang, J.Z., Burrow, S., Neild, S. and Conn A. [2021] "Using an inerter to enhance an active-passive-combined vehicle suspension system," *International Journal of Mechanical Sciences* **204**, 106535.

Lei, X., Wu, C. and Wu, H. [2018] "A novel composite vibration control method using double-decked floating raft isolation system and particle damper," *Journal of Vibration and Control* **24**(19), 4407-4418.

Li, Y. and Xu, D. [2018] "Force transmissibility of floating raft systems with quasi-zero-stiffness isolators," *Journal of Vibration and Control* **24**(16), 3608-3616.

Liu, Y., Yang, J., Yi, X., Chronopoulos, D. [2022] "Enhanced suppression of low-frequency vibration transmission in metamaterials with linear and nonlinear inerters," *Journal of Applied Physics* **131**(10), 105103.

Lu, Z.Q., Brennan, M.J. and Chen, L.Q. [2016] "On the transmissibilities of nonlinear vibration isolation system," *Journal of Sound and Vibration* **375**, 28-37.

Matichard, F., Lantz, B., Mason, K., Mittleman, R., Abbott, B., Abbott, S., Allwine, E.,Barnum, S., Birch, J.,Biscans, S., Clark, D.,Coyne, D., DeBra, D., DeRosa, R., Foley, S., Fritschel, P., Giaime, J. A.,Gray, C., Grabeel, G., Hanson, J., Hillard, M., Kissel, J., Kucharczyk, C., Le Roux, A., Lhuillier, V., Macinnis, M., O'Reilly, B., Ottaway, D., Paris, H., Puma, M., Radkins, H., Ramet, C., Robinson, M., Ruet, L., Sareen, P., Shoemaker, D., Stein, A., Thomas, J., Vargas, M., Warner, J. [2015] "Advanced LIGO two-stage twelve-axis vibration isolation and positioning platform. Part 1: Design and production overview," *Precision Engineering* **40**, 273-286.

Morales, C. A. [2022] "Inerter-added transmissibility to control base displacement in isolated structures," *Engineering Structures* **251**, 113564.

Niu, M.Q. and Chen, L.Q. [2022] "Analysis of a bio-inspired vibration isolator with a compliant limb-like structure," *Mechanical Systems and Signal Processing* **179**, 109348.

Yan, B., Yu, N., Ma, H.Y. and Wu, C.Y. [2022] "A theory for bistable vibration isolators," *Mechanical Systems and Signal Processing* **167**, 108507.

Qiu, Y., Xu, W., Bu, W. and Qin, W. [2022] "Raft attitude control and elastic deformation suppression technique for large-scale floating raft air spring mounting system," *Journal of Vibration and Control* **28**(23-24), 3457-3468.

Renno, J., Sondergaard, N., Sassi, S. and Paurobally, M. R. [2019] "Wave scattering and power flow in straight-helical-straight waveguide structure," *International Journal of Applied Mechanics* **11**(8), 1950075.

Shi, B.Y., Dai, W., Yang, J. [2022] "Performance analysis of a nonlinear inerter-based vibration isolator with inerter embedded in a linkage mechanism." *Nonlinear Dynamics* **109**(2), 419-442

Shi, B.Y., Yang, J. and Jiang, J.Z. [2022] "Tuning methods for tuned inerter dampers coupled to nonlinear primary systems," *Nonlinear Dynamics* **107**(2), 1663-1685.

Smith, M.C. [2002] Synthesis of mechanical networks: The inerter. *IEEE Transactions on Automatic Control* **47**(10), 1648– 1662.

Wang, X., Zhou, J., Xu, D., Ouyang, H. and Duan, Y. [2017] "Force transmissibility of a two-stage vibration isolation system with quasi-zero stiffness," *Nonlinear Dynamics* **87**(1), 633-646.

Wang, Y., Du, J. and Cheng, L. [2019] "Power flow and structural intensity analyses of acoustic black hole beams," *Mechanical Systems and Signal Processing* **131**, 538-553.

Wang, Y., Li, H., Cheng, C., Ding, H., Chen, L. [2020] "Dynamic performance analysis of a mixed-connected inerter-based quasi-zero stiffness vibration isolator," *Structural Control and Health Monitoring* **27**(10), e2604.

Wang, Y., Li S., Neild, S.A. and Jiang, J.Z. [2017] "Comparison of the dynamic performance of nonlinear one and two degree-of-freedom vibration isolators with quasi-zero stiffness," *Nonlinear Dynamics* **88**(1), 635-654.

Wang, Y., Wang, R. C. and Meng, H. D. [2018] "Analysis and comparison of the dynamic performance of one-stage inerter-based and linear vibration isolators," *International Journal of Applied Mechanics* **10**(1), 1850005.

Wang, Y., Wang, P., Meng, H., Chen L. [2022] "Nonlinear vibration and dynamic performance analysis of the inerter-based multi-directional vibration isolator," *Archive of Applied Mechanics* **92**(12), 3597-3629.

Xie, X., Ren, M., Zheng, H. and Zhang, Z. [2019] "Investigation on a two-stage platform of large stroke for broadband vertical vibration isolation," *Journal of Vibration and Control* **25**(6), 1233-1245.

Yang, J., Jiang, J.Z. and Neild, S.A. [2019] "Dynamic analysis and performance evaluation of nonlinear inerter-based vibration isolators," *Nonlinear Dynamics* **99**(3), 1823-1839.

Yang, J., Jiang J.Z., Zhu, X., Chen, H. [2017] "Performance of a dual-stage inerter-based vibration isolator," *Procedia engineering* **199**, 1822-1827.

Yang, T., Wu, L., Li, X., Zhu, M., Liu, Z. and Brennan, M.J. [2021] "Combining active control and synchrophasing for vibration isolation of a floating raft system: An experimental demonstration," *Journal of Low Frequency Noise, Vibration and Active Control* **40**(2), 1105-1114.

Ye, K., and Ji, J. C. [2022] "An origami inspired quasi-zero stiffness vibration isolator using a novel truss-spring based stack Miura-ori structure," *Mechanical Systems and Signal Processing* **165**, 108383.

Zhang, S.Y., Neild, S. and Jiang, J.Z. [2020] "Optimal design of a pair of vibration suppression devices for a multi-storey building," *Structural Control and Health Monitoring* **27**(3), 2498.

Zhang, Y. W., Gao, C. Q., Zhang, Z. and Zang, J. [2021] "Dynamic analysis of vibration reduction and energy harvesting using a composite cantilever beam with galfenol and a nonlinear energy sink," *International Journal of Applied Mechanics* **13**(8), 1950100.

Zhang, X., Yang, Y., Ma, H., Shi, M., and Wang, P. [2023] "A novel diagnosis indicator for rub-impact of rotor system via energy method," *Mechanical Systems and Signal Processing* **185**, 109825.

Zhao, F., Ji, J.C., Ye, K. and Luo, Q. [2020] "Increase of quasi-zero stiffness region using two pairs of lateral springs," *Mechanical Systems and Signal Processing* **144**, 106975.

Zhao, X. Y., Zhang, Y. W., Ding, H. and Chen, L. Q. [2018] "Vibration suppression of a nonlinear fluid-conveying pipe under harmonic foundation displacement excitation via nonlinear energy sink," *International Journal of Applied Mechanics,* **10**(9), 1850096.

Zhao, Z., Zhang, R., Wierschem, N.E., Jiang, Y. and Pan, C. [2021] "Displacement mitigation–oriented design and mechanism for inerter-based isolation system," *Journal of Vibration and Control* **27**(17-18), 1991-2003.

Zhu, C., Yang, J., Rudd, C. [2021] "Vibration transmission and power flow of laminated composite plates with inerter-based suppression configurations" *International Journal of Mechanical Sciences* **190**, 106012.